Supplementary Information

Engineering ultrafast exciton dynamics to boost organic photovoltaic performance

Yu Guo,[1,#] Guangchao Han,[2,#] Jing Guo,[3] Haotian Guo,[3] Yuang Fu,[4] Xiaodan Miao, [2] Zhen Wang,[1] Dongsheng Li,[1] Shuixing Li,[5] Xiaomin Xu,[3] Xinhui Lu,[4] Hongzheng Chen,[5] Yuanping Yi,[2,*] Philip C. Y. Chow[1,*]

1. Department of Mechanical Engineering, The University of Hong Kong, Pokfulam, Hong Kong, China

2. CAS Key Laboratory of Organic Solids, Institute of Chemistry, Chinese Academy of Sciences, Haidian, Beijing, China

3. Institute of Materials Research, Shenzhen International Graduate School, Tsinghua University, Shenzhen, China

4. Department of Physics, The Chinese University of Hong Kong, Shatin, Hong Kong, China

5. State Key Laboratory of Silicon and Advanced Semiconductor Materials, International Research Center for X Polymers, Department of Polymer Science and Engineering, Zhejiang University, Hangzhou, China

# These authors contributed equally

*Correspondence to P. C. Y. Chow <pcyc@hku.hk>, Y. Yi <ypyi@iccas.ac.cn>

Contents

Supplementary Note 1. Extended notes on transient electroabsorption (TEA) signal analysis

As discussed in main text, the TA spectral shift of Y-type acceptor neat films is due to the presence of transient electroabsorption (TEA) response. Such TEA response is caused by the electric field formed between separated electrons and holes of intermolecular charge-transfer (ICT) states in ordered regions of molecular aggregates. In comparison, the TA spectral shift around the absorption edge of Y-type acceptors with increasing pump-probe time delay is more significant in D-A blend films (e.g. TA spectral shift from ~833 to 849 nm in PM6:Y6 film; **Supplementary Fig. 15a**), indicating stronger TEA signals, compared to that in neat films (e.g. TA spectral shift from ~854 to 860 nm in Y6 film; **Supplementary Fig. 1**). The stronger TEA signals in D-A blends arise from the free-polaron-induced Stark shift as electrons and holes are fully separated across the D-A interface, where the electric field between fully separated electron-hole pairs can affect more molecules than that by ICT states in neat films. This is confirmed by the matched growth kinetics of TEA signals in blend films and that of polaron absorption, with growth up to ~100 ps (**Supplementary Fig. 15**). As a result, the TEA signal growth due to exciton migration within Y-type acceptor domains in blend films is masked by the significantly stronger TEA signals contributed by the generation of free charges. Therefore, it is challenging to trace the TEA signal growth in PM6:Y-type acceptor blend films to study the structure-energy landscape of Y-type acceptor aggregates.

As mentioned above, the reason for the applicability of the TEA method to study the exciton migration from disordered to ordered regions in Y-type acceptor neat films is the relatively strong EA signal intensity in ordered molecular packing regions contributed by the formation of delocalized ICT states in contrast to the weak EA signal

in disordered regions. The formation of ICT states in Y-type acceptor aggregates results from their strong intermolecular electronic coupling. In contrast, the intermolecular electronic coupling is weak in ITIC-type acceptor films where excitons are localized[1,2]. Therefore, this TEA method may not be applicable to study ITIC-type acceptors.

Supplementary Note 2. Determination of the time (τ) for change in transient EA (ΔTEA) signal to reach the maximum intensity

In main text, we define τ as the time taken for the ΔTEA signal to reach the maximum intensity. ΔTEA signal is the change in TEA signal intensity with respect to that early time (0.2 ps), i.e., the growth dynamics of ΔTEA signal starts at 0.2 ps. Therefore, τ is the time difference between the time at which ΔTEA signal reaches the maximum intensity and 0.2 ps. For example, for a Y6 film, ΔTEA signal reaches the maximum intensity at time delay of 2.75 ps, then τ = 2.75 ps – 0.2 ps = 2.55 ps. Because of the fluctuation of the ΔTEA kinetics, there can be a range for estimating the time at which ΔTEA signal reaches the maximum intensity. Accordingly, there is a range for estimating τ, i.e. τ_{min} and τ_{max}, which were determined by plotting ΔTEA growth kinetics with time delay in linear scale (**Supplementary Fig. 11**). Therefore, we can obtain a pair of τ_{min} and τ_{max} for one film sample. The τ values used in **Figs. 3c-f** in main text were averaged from τ_{min} and τ_{max} of five film samples for each Y-type acceptor and can be found in **Supplementary Table 1**.

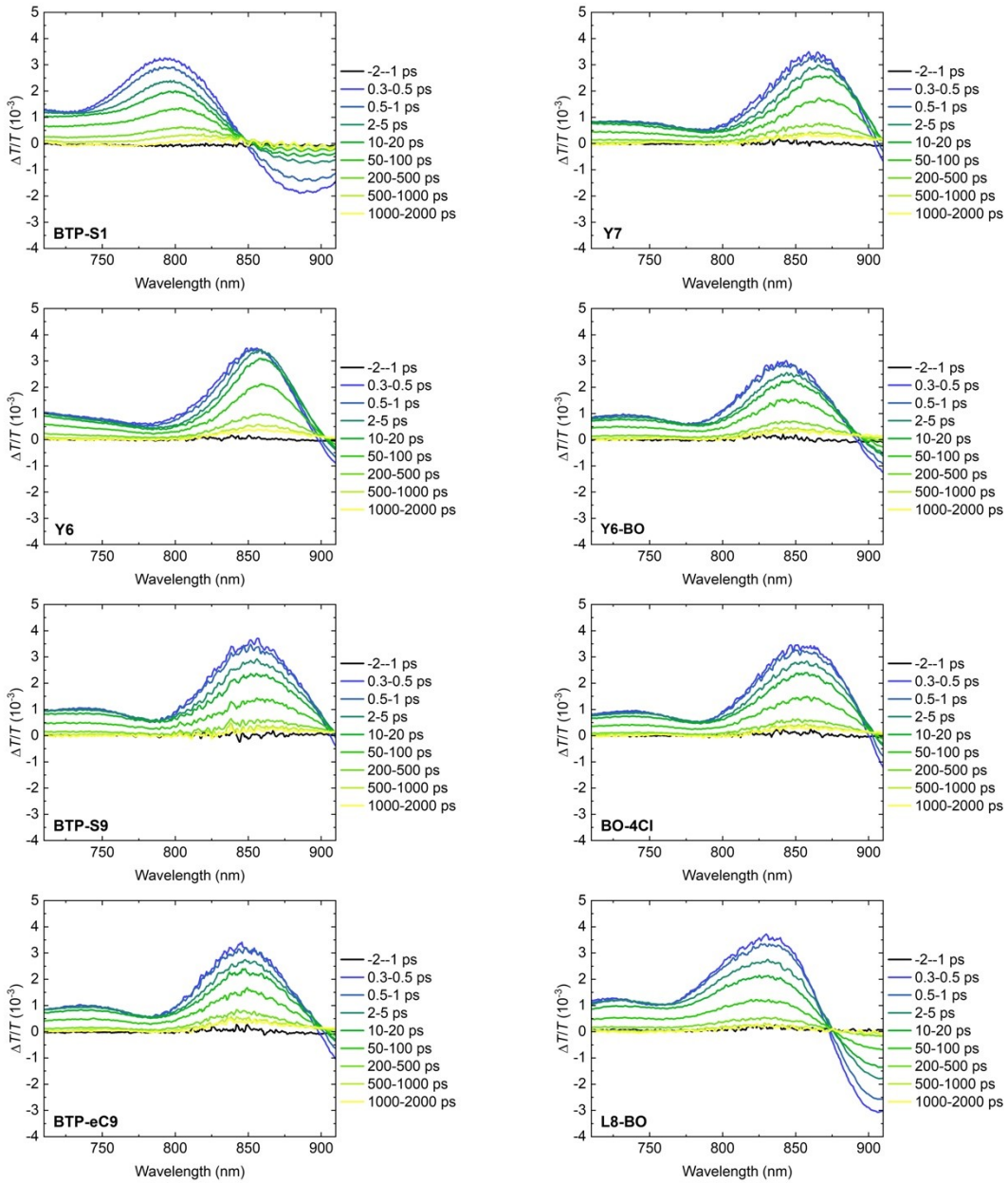

Supplementary Figure 1. Transient absorption spectra of Y-type acceptor neat films pumped at 700 nm with fluence of ~4.5 μJ cm^{-2}.

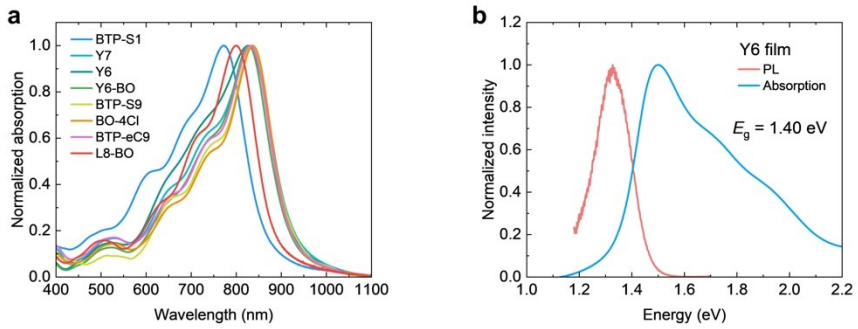

Supplementary Figure 2. (a) Ground-state absorption spectra of Y-type acceptor neat films. (b) Absorption and photoluminescence (PL) spectra of Y6 neat film. The optical bandgap (E_g) is determined from the intersection of absorption and PL spectra.

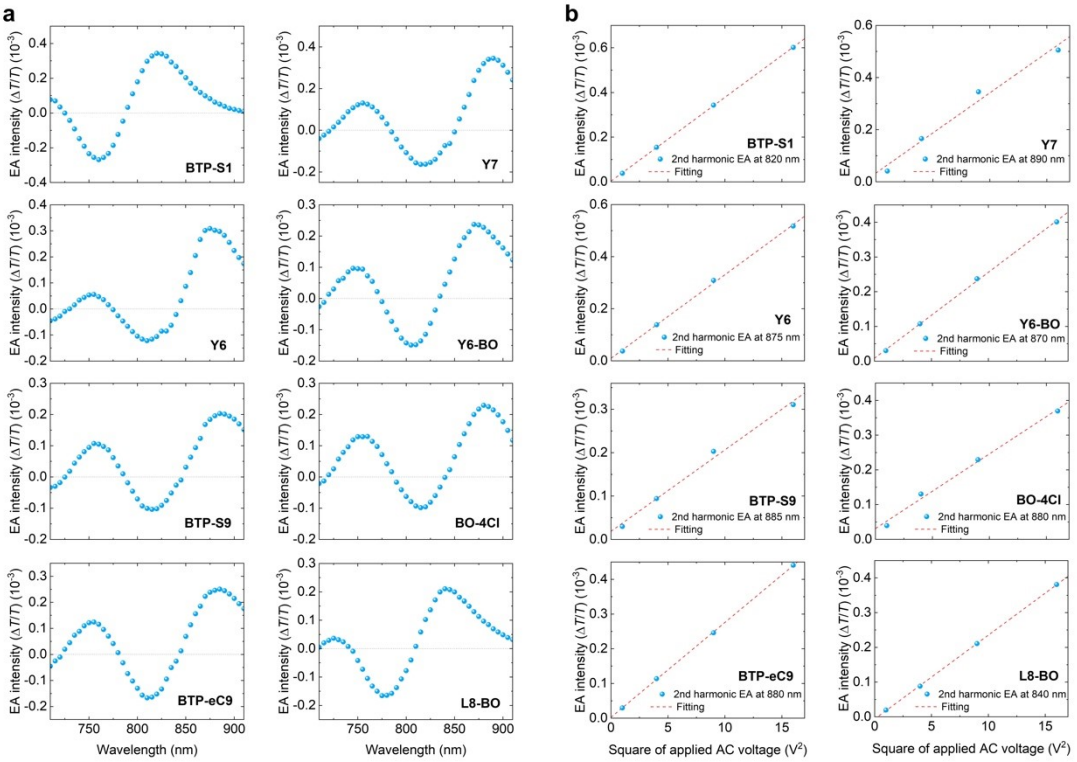

Supplementary Figure 3. The steady-state second (2nd) harmonic electroabsorption (EA) spectra of Y-type acceptor-neat-film-based devices at an applied alternating current (AC) voltage of 3 V (a) and peak intensity at different applied AC voltages (b). The 2nd harmonic EA intensity of Y-type acceptors shows a linear relationship with the square of applied AC voltage, i.e. indicating the quadratic dependence of the 2nd harmonic EA intensity on the applied AC electric field, which is in agreement with the Stark effect[3,4].

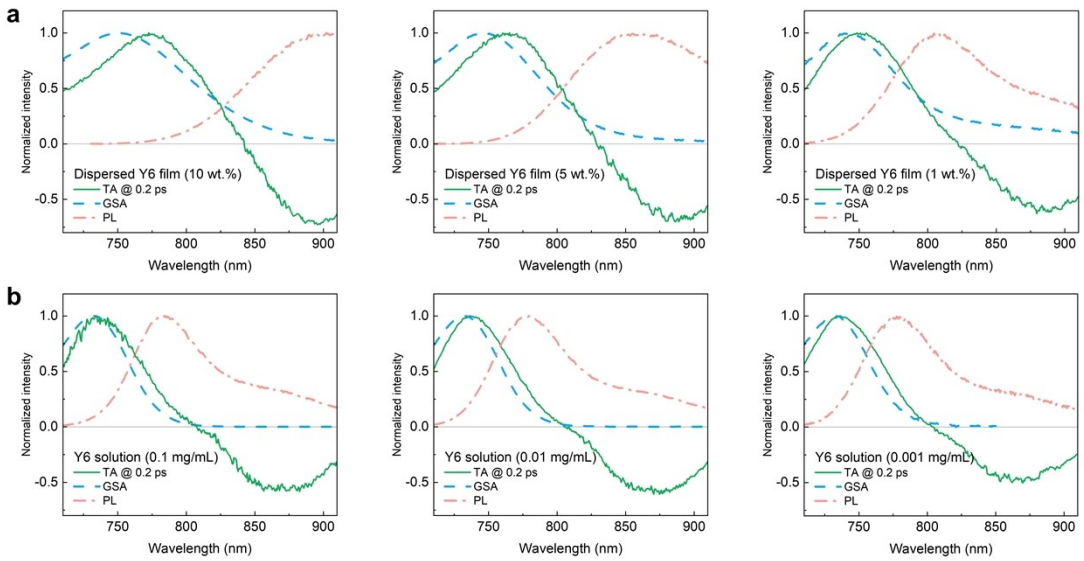

Supplementary Figure 4. Comparison between transient absorption (TA) spectra at 0.2 ps, ground-state absorption (GSA) and photoluminescence (PL) spectra of dispersed films in polymer matrix (polyvinyl carbazole, PVK) (a) and solutions (b) of Y6.

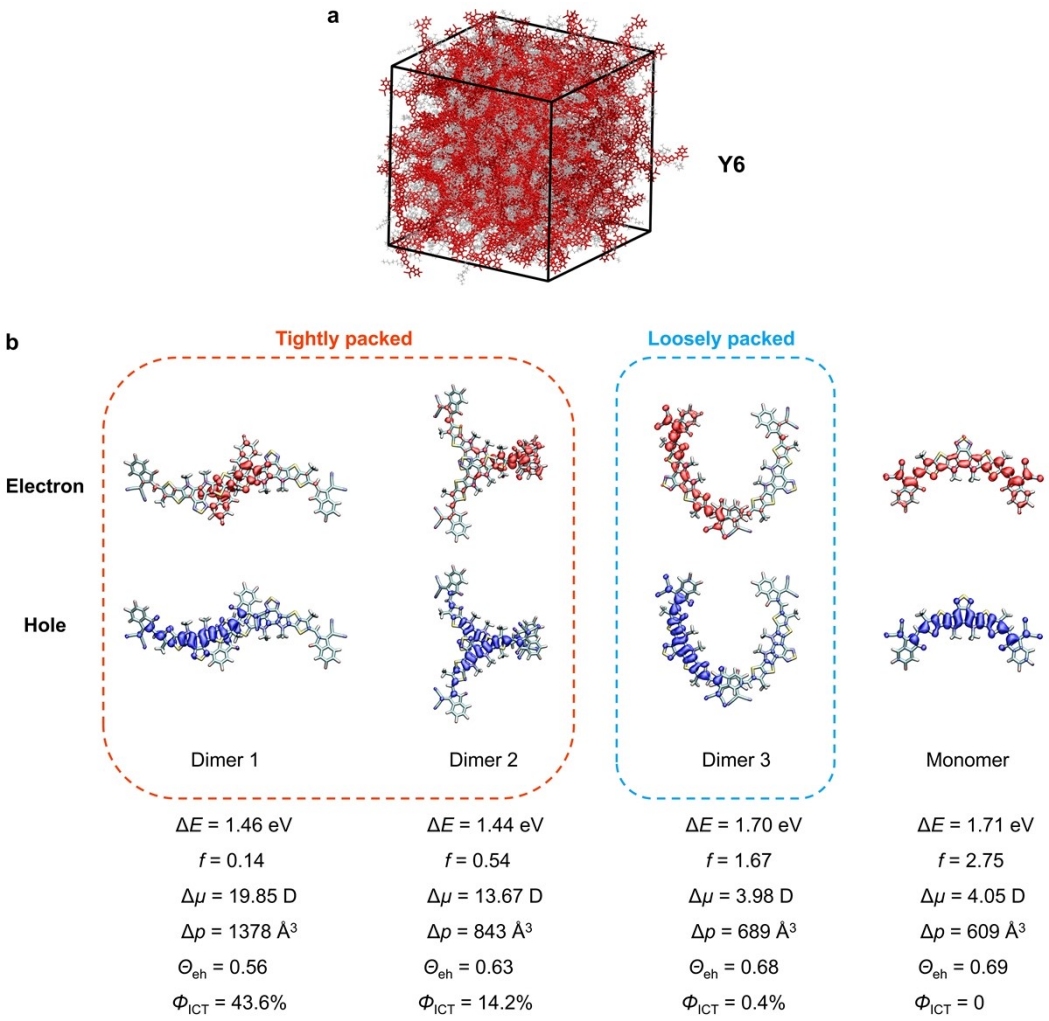

Supplementary Figure 5. (a) Representative molecular packing morphology of the MD-simulated Y6 film (backbone: red). The long side chains were replaced with methyl groups in our time-dependent DFT calculations. (b) Top: Electron and hole density distributions for the lowest singlet excited states (S_1 states) of representative dimers and monomer of Y6 in MD simulated film. Bottom: Calculated energies (ΔE), oscillator strengths (f), change in dipole moment ($\Delta\mu$) and polarizability (Δp) from ground states to excited states, electron-hole overlap (Θ_{eh}) and apparent intermolecular charge-transfer (ICT) percentage (Φ_{ICT}) for the S_1 states of representative dimers and monomer of Y6.

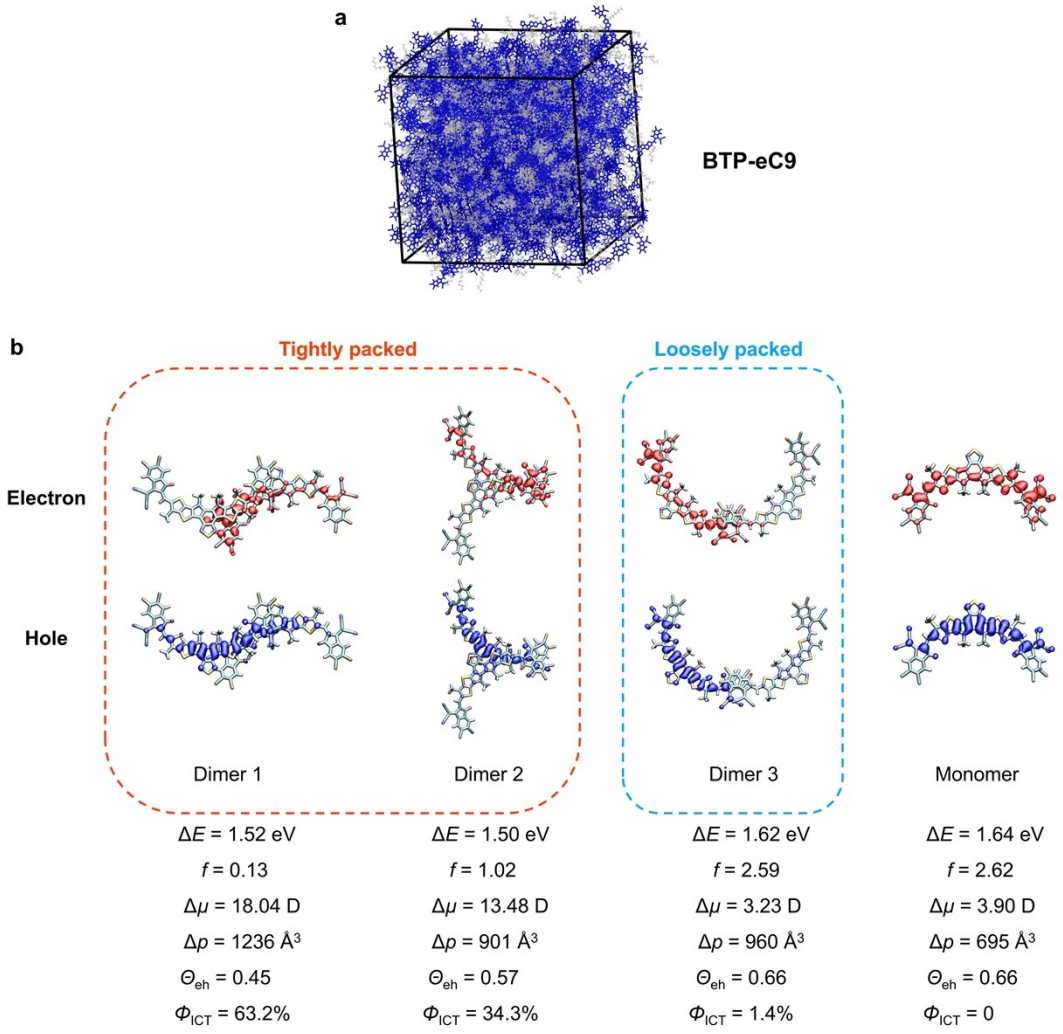

Supplementary Figure 6. (a) Representative molecular packing morphology of the MD-simulated BTP-eC9 film (backbone: blue). The long side chains were replaced with methyl groups in our time-dependent DFT calculations. (b) Top: Electron and hole density distributions for the lowest singlet excited states (S_1 states) of representative dimers and monomer of BTP-eC9 in MD simulated film. Bottom: Calculated energies (ΔE), oscillator strengths (f), change in dipole moment ($\Delta\mu$) and polarizability (Δp) from ground states to excited states, electron-hole overlap (Θ_{eh}) and apparent intermolecular charge-transfer (ICT) percentage (Φ_{ICT}) for the S_1 states of representative dimers and monomer of BTP-eC9.

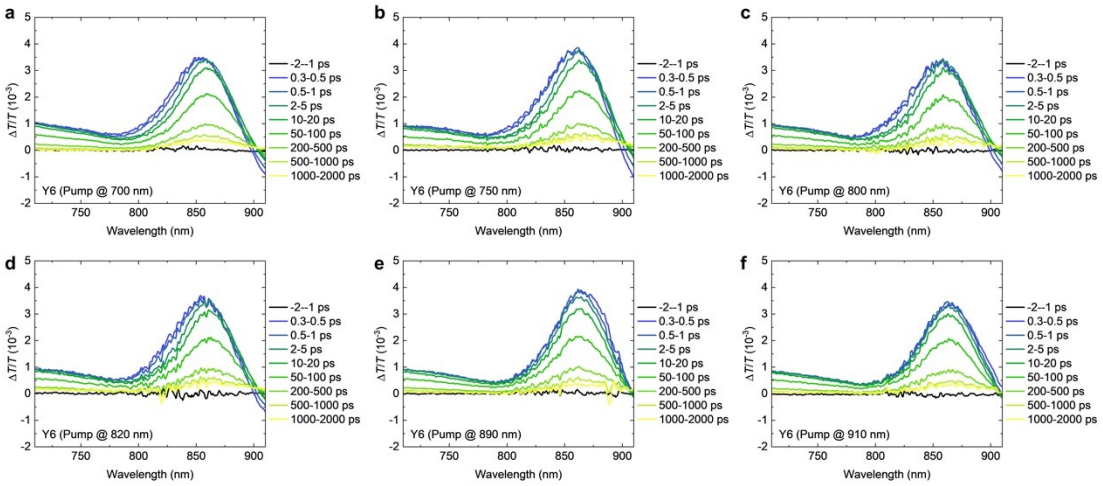

Supplementary Figure 7. Transient absorption spectra of Y6 neat film with pump at 700 nm (a), 750 nm (b), 800 nm (c), 820 nm (d), 890 nm (e), and 910 nm (f).

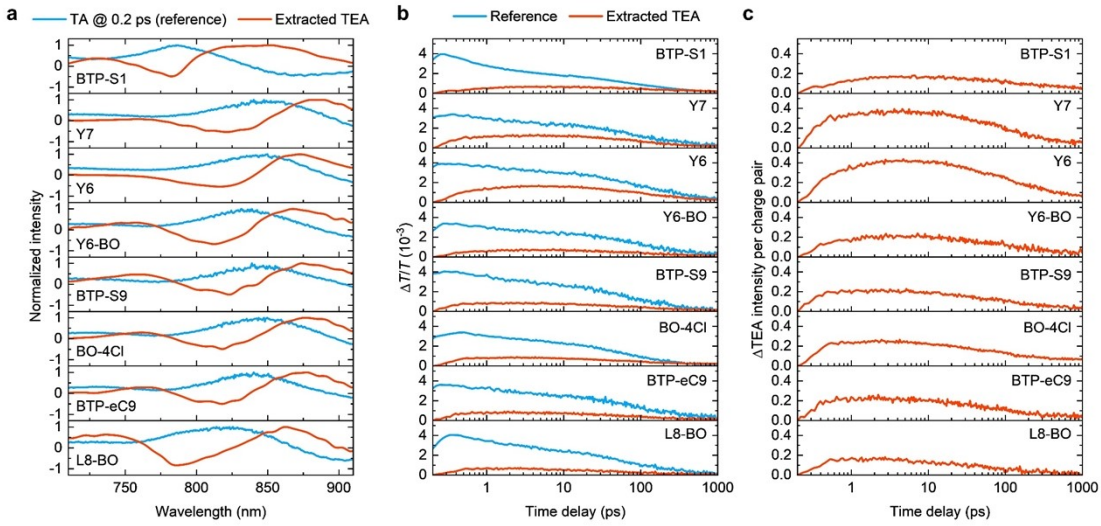

Supplementary Figure 8. (a) Transient absorption (TA) spectra at 0.2 ps and transient electroabsorption (TEA) spectra extracted by genetic algorithm (GA) from time-dependent TA spectra of Y-type acceptor neat films pumped at 700 nm. According to the discussion in main text, the TA spectra at 0.2 ps of Y-type acceptors already have contributions from TEA responses (due to the formation of intermolecular charge-transfer states in Y-type acceptor aggregates) in addition to ground-state bleaching signals. For the spectral decomposition of TA data using GA, the TA spectrum at 0.2 ps was used as the reference signal, and GA was used to extract the other component, i.e. the TEA signal, together with the kinetics of the reference and TEA signals. (b) Kinetics of the reference and TEA signals generated by GA. The intensity of the extracted TEA signal is actually the change in TEA (ΔTEA) signal intensity relative to the initial TEA intensity at 0.2 ps. As discussed in main text, the growth in TEA signals of Y-type acceptors arises from the migration of excited states from local excitons (LEs) in disordered regions to intermolecular charge-transfer (ICT) states in ordered regions. (c) Kinetics of change in TEA (ΔTEA) intensity per charge pair (normalized TEA intensity to the maximum reference signal intensity) of Y-type acceptor neat films.

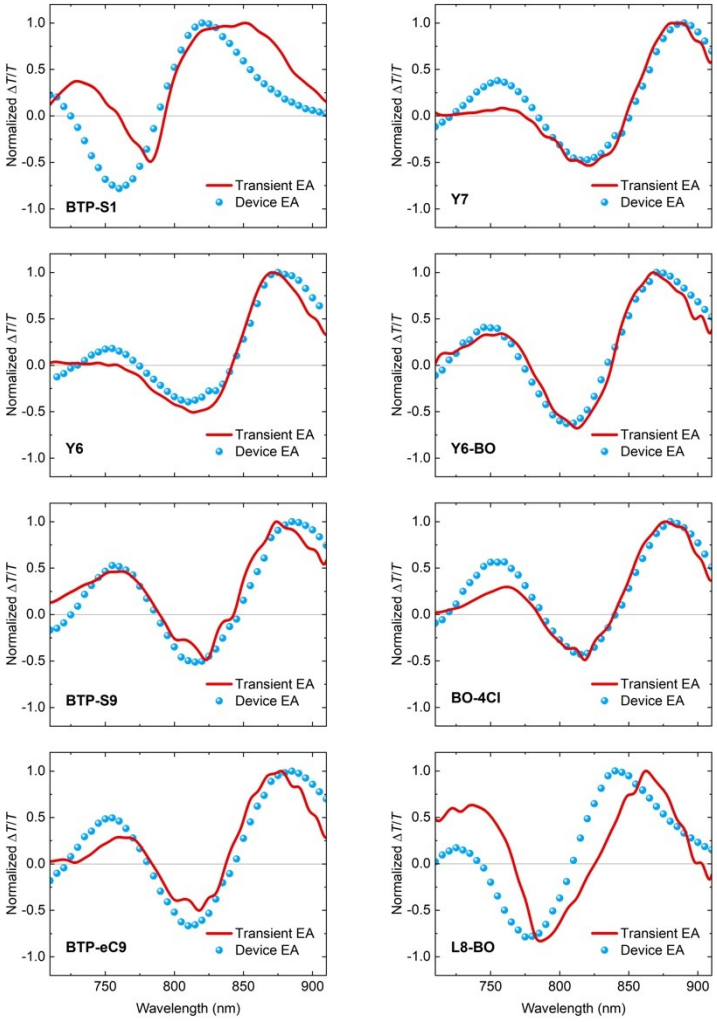

Supplementary Figure 9. Comparison between transient electroabsorption (EA) and steady-state device EA spectra of Y-type acceptor neat films. The transient EA and steady-state device EA spectra show a good match for most Y-type acceptors except BTP-S1 and L8-BO. The small difference between transient EA spectra of BTP-S1 and L8-BO and their device EA spectra may be due to their relatively low intensity of growth in transient EA signals (i.e. small structural difference between disordered and ordered regions), which affects the accuracy of extraction by genetic algorithm (GA). According to GIWAXS structural characterizations (see **Supplementary Fig. 20b**), BTP-S1 neat film has a broad polar angle distribution, indicating the low degree of molecular orientation and overall structural order. In contrast, L8-BO neat film exhibits a narrow polar angle distribution, indicating oriented molecules and high degree of overall structural order.

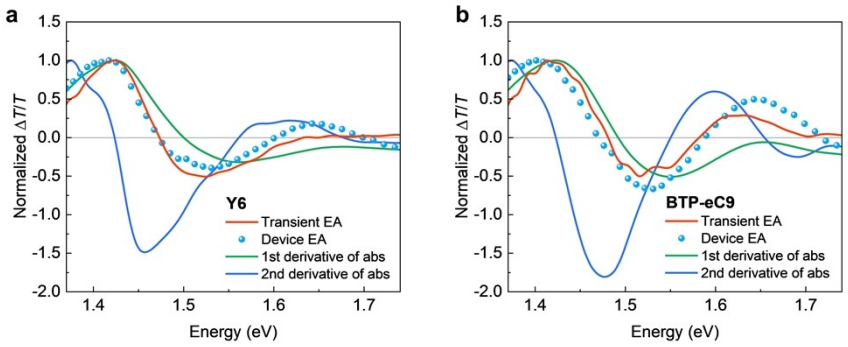

Supplementary Figure 10. Transient electroabsorption (EA) and steady-state device EA spectra, and the first and second derivatives of absorption spectra of (a) Y6 and (b) BTP-eC9 films.

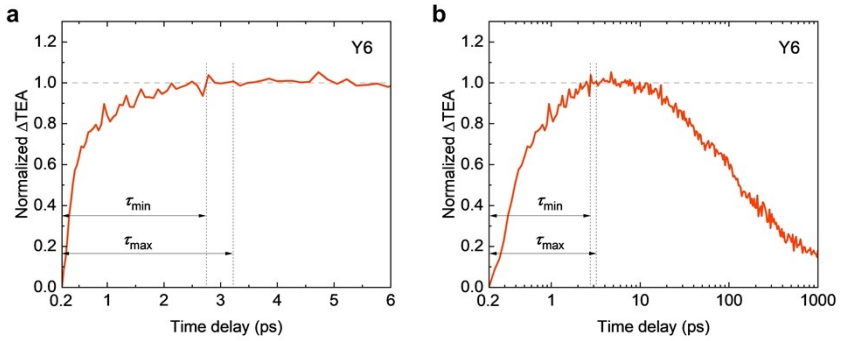

Supplementary Figure 11. (a) Schematics of determining the range of ΔTEA growth time, τ (τ_{min} and τ_{max}) for Y6 film, by plotting ΔTEA signal kinetics with time delay in linear scale. (b) τ_{min} and τ_{max} of Y-type acceptors in plot of ΔTEA signal kinetics with time delay in logarithmic scale. The τ values used in **Figs. 3c-f** in main text were averaged from τ_{min} and τ_{max} of five film samples for each Y-type acceptor and can be found in **Supplementary Table 1**.

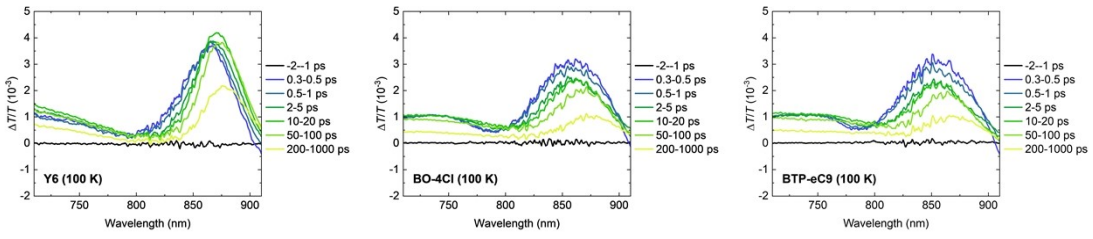

Supplementary Figure 12. Transient absorption spectra of Y-type acceptor neat films measured at temperature of 100 K with pump at 700 nm with fluence of ~4.5 μJ cm^{-2}.

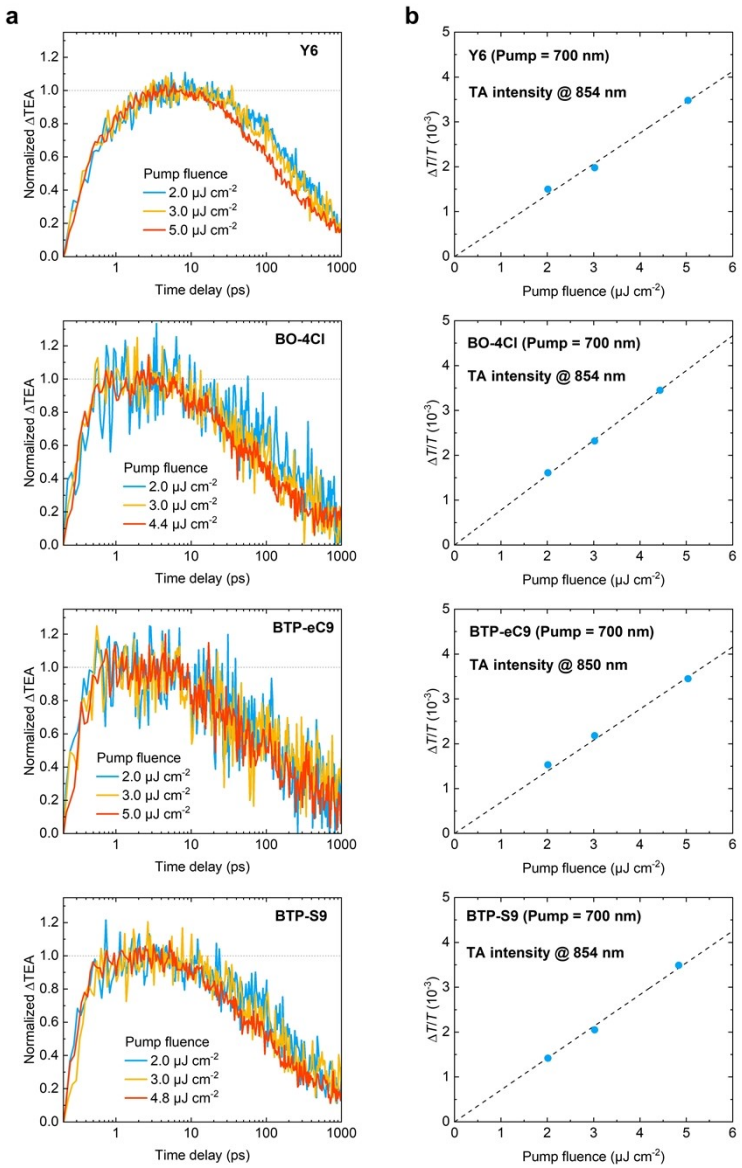

Supplementary Figure 13. Kinetics of change in transient electroabsorption (ΔTEA) signals (a) and transient absorption (TA) spectral peak intensity at 0.2 ps (b) of Y6, BO-4Cl, BTP-eC9 and BTP-S9 neat films pumped at 700 nm with a range of fluences.

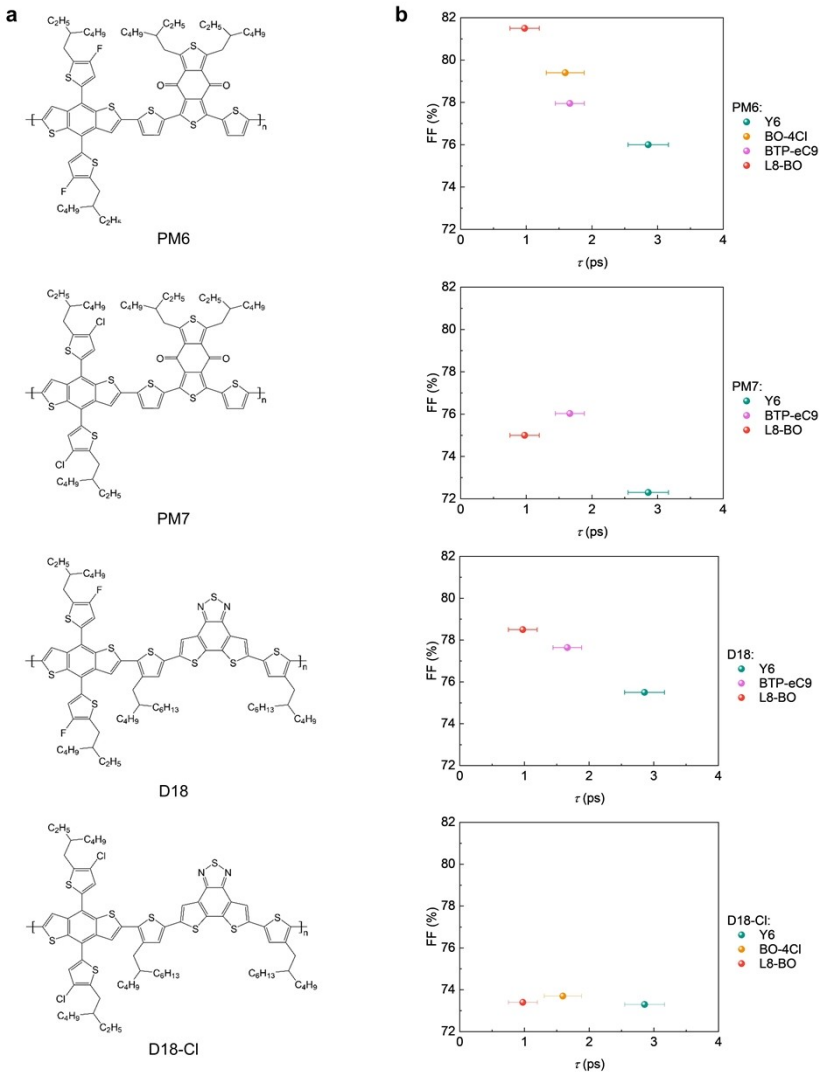

Supplementary Figure 14. (a) Chemical structure of donor polymers, PM6 (PBDB-T-2F), PM7, D18 and D18-Cl. (b) Plots of fill factor (FF) of binary organic solar cells based on Y-type acceptors and various donor polymers, PM6, PM7, D18 and D18-Cl, with respect to ΔTEA growth time (τ) of Y-type acceptor neat films. The fill factor values used here are those of the best-performance devices reported in literature. The summary of the device performance can be found in **Supplementary Table 4**. Blend devices based on PM6, PM7 and D18 show a general trend of higher fill factor for Y-type acceptor with shorter τ, consistent with the trend discussed in main text. The exception is blend devices based on D18-Cl, where all three blend systems have relatively low fill factor, possibly resulting from the over-aggregation of D18-Cl[5,6].

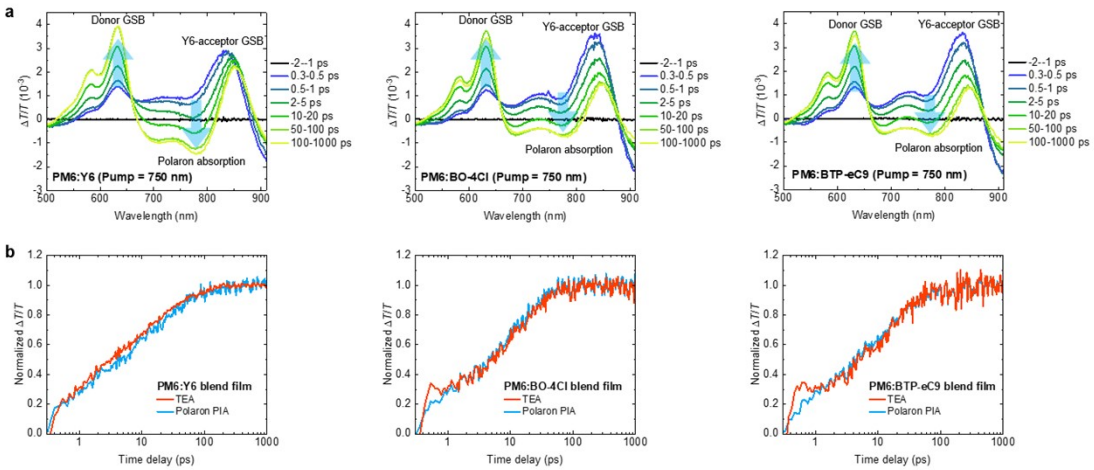

Supplementary Figure 15. (a) Transient absorption spectra of PM6:Y-type acceptor blend films pumped at 750 nm with fluence of ~3.0 μJ cm^{-2}, selectively exciting the acceptor. There is a growth in donor ground-state bleach (GSB; ~550-650 nm) signal up to ~100 ps, indicating the hole transfer from Y-type acceptor to donor PM6. In addition, there is a growth of polaron absorption signal (~670-800 nm) indicating formation of D-A charge-transfer states and charge generation, which overlaps with Y-type acceptor GSB. The charge generation takes place up to ~100 ps, consistent with previous work[7,8]. (b) Kinetics of the photoinduced absorption (PIA) of polarons and extracted transient electroabsorption (TEA) signals in PM6:Y-type acceptor blend films. The growth kinetics of TEA signals agrees well with that of the polaron PIA signals, indicating that the growth of TEA signals in blend films is mainly contributed by the formation of free charges.

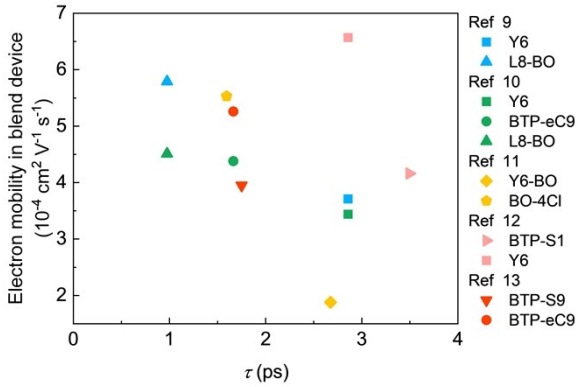

Supplementary Figure 16. Electron mobility of PM6:Y-type acceptor blend devices reported from literature[9-13] with respect to ΔTEA growth time (τ) of Y-type acceptor neat films. Within the same literature, Y-type acceptors with shorter τ of neat films generally tend to achieve higher electron mobility in blend films with donor polymer PM6.

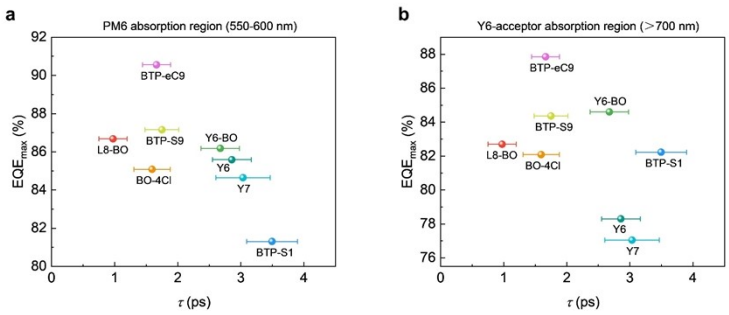

Supplementary Figure 17. Plots of maximum external quantum efficiency (EQE_{max}) of binary organic solar cells in absorption regions of donor PM6 (a) and Y-type acceptors (b) with respect to τ of Y-type acceptor neat films.

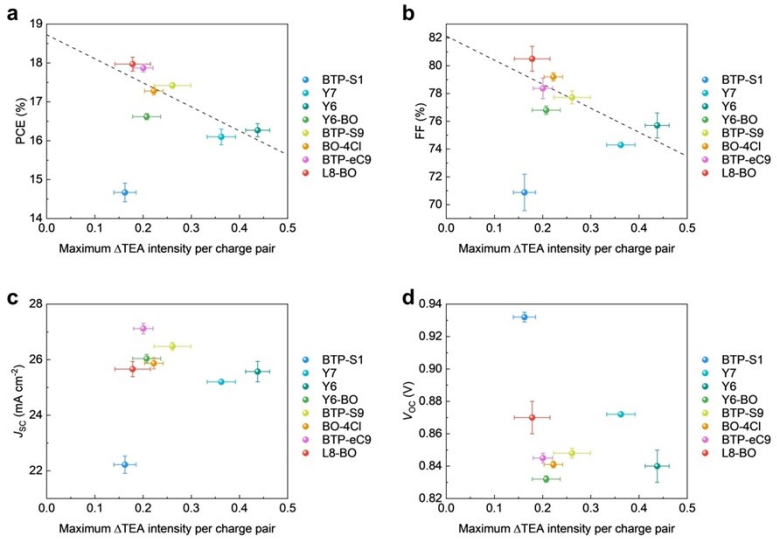

Supplementary Figure 18. Plots of power conversion efficiency (PCE) (a), fill factor (FF) (b), short-circuit current density (J_{SC}) (c), open-circuit voltage (V_{OC}) (d) of binary organic solar cells based on donor polymer PM6 and Y-type acceptors with respect to the maximum ΔTEA intensity per charge pair of Y-type acceptor neat films. The performance parameters of OSC devices are collected from literature[9,11-15]. The maximum ΔTEA intensity per charge pair values used here were averaged from five samples for each Y-type acceptor and can be found in **Supplementary Table 1**. As discussed in main text, the growth in TEA signals of Y-type acceptors arises from the migration of excited states from local excitons (LEs) in disordered regions to intermolecular charge-transfer (ICT) states in ordered regions. Therefore, the maximum ΔTEA intensity per charge pair (ΔTEA_{max}) provides a measure of the overall contrast between disordered and ordered regions of the film. There is a general trend of higher PCE/FF in blend devices for Y-type acceptors with smaller ΔTEA_{max}, indicating that Y-type acceptors with smaller structural difference between the disordered and ordered regions, i.e. more uniform structures, are beneficial to the charge transport and thus fill factor and efficiency of blend devices. However, the blend devices based on BTP-S1, which has a relatively small ΔTEA_{max}, exhibit low PCE and FF. According to GIWAXS structural characterizations (see **Supplementary Fig. 20b**), BTP-S1 neat film has the broadest polar angle distribution among studied Y-type acceptors, indicating the least orientation of molecules. Therefore, while the relatively small ΔTEA_{max} of BTP-S1 indicates a small structural difference between the

disordered and ordered regions, its broad polar angle distribution reveals the low degree of overall structural order. Therefore, uniform and ordered structures of Y-type acceptor aggregates are important to achieving high fill factor and efficiency in blend devices.

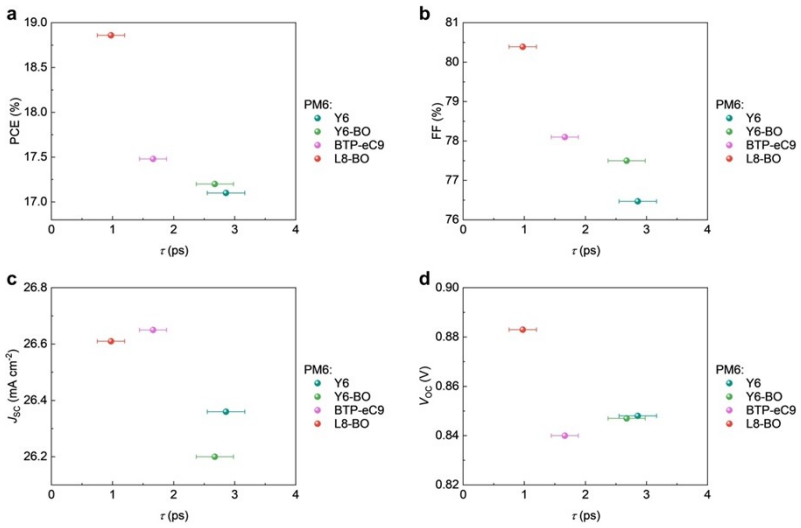

Supplementary Figure 19. Plots of power conversion efficiency (PCE) (a), fill factor (FF) (b), short-circuit current density (J_{SC}) (c), and open-circuit voltage (V_{OC}) (d) of binary organic solar cells based on donor polymer PM6 and Y-type acceptors prepared via layer-by-layer (LBL) approach with respect to ΔTEA growth time (τ) of Y-type acceptor neat films. The photovoltaic performance parameters used here are those of the best-performance devices reported in literature. The summary of the device performance can be found in **Supplementary Table 5**.

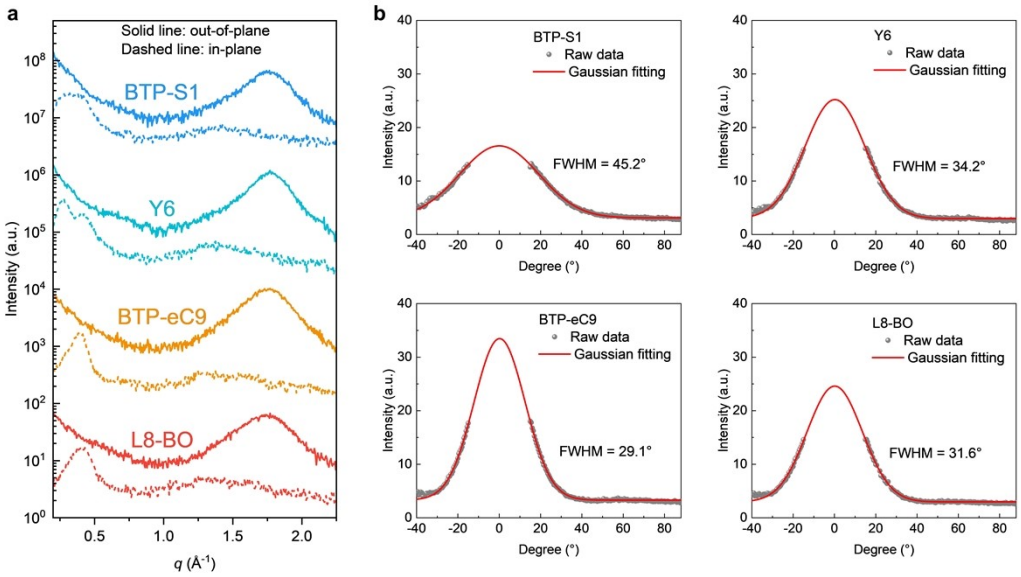

Supplementary Figure 20. (a) Grazing-incidence wide-angle X-ray scattering (GIWAXS) line-cut profiles in in-plane and out-of-plane directions of Y-type acceptor neat films. (b) Polar angle distribution of π-π stacking peak and Gaussian fitting of full width at half maximum (FWHM) of Y-type acceptor neat films. The narrower polar angle distribution (smaller FWHM) indicates more oriented molecules.

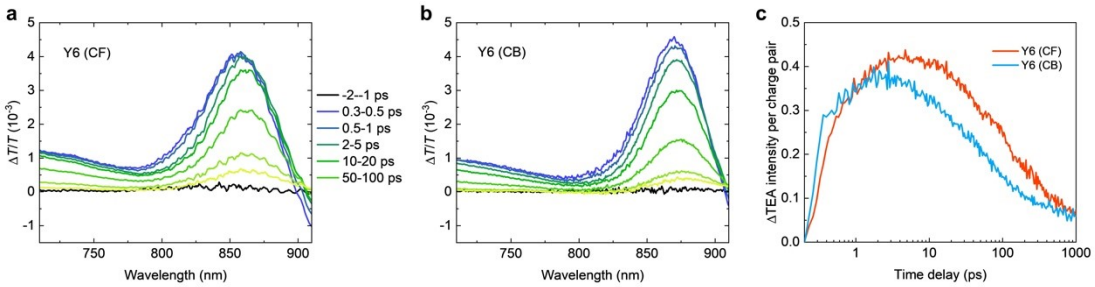

Supplementary Figure 21. Transient absorption spectra of Y6 neat films spin-coated from chloroform (CF) (a) and chlorobenzene (CB) (b) solutions with pump at 700 nm and fluence of ~5.0 μJ cm^{-2}. (c) Kinetics of change in transient electroabsorption (ΔTEA) signals of Y6 neat films prepared from CF and CB solutions. As reported before[16,17], Y6 (CB) film has more edge-on-orientations of molecules and thus more mixed orientations with energetic offset than Y6 (CF) film. As a result, free charge generation is more efficient in Y6 (CB) film than in Y6 (CF) film upon photoexcitation. It is expected that the maximum ΔTEA intensity in Y6 (CB) film should be higher than that in Y6 (CF) film if the ΔTEA signal is mainly contributed by free

charge generation. However, Y6 (CB) film shows similar or even a bit lower maximum ΔTEA intensity than that of Y6 (CF) film. Therefore, free chare generation in Y6 neat films is not the main contribution to the ΔTEA signals.

Supplementary Table 1. ΔTEA growth time (τ) and maximum intensity per charge pair (ΔTEA_{max}) of Y-type acceptor neat films.

Y-type acceptors	τ (ps)	ΔTEA_{max}
BTP-S1	3.50 ± 0.40	0.162 ± 0.023
Y7	3.04 ± 0.43	0.362 ± 0.030
Y6	2.86 ± 0.31	0.438 ± 0.025
Y6-BO	2.68 ± 0.30	0.207 ± 0.029
BTP-S9	1.75 ± 0.27	0.261 ± 0.038
BO-4Cl	1.59 ± 0.29	0.222 ± 0.019
BTP-eC9	1.66 ± 0.22	0.201 ± 0.020
L8-BO	0.98 ± 0.22	0.178 ± 0.037

Note:

(1) τ and ΔTEA_{max} for each Y-type acceptor are averaged from 5 film samples.

Supplementary Table 2. Photovoltaic parameters of PM6:Y-type acceptor blend-based devices collected from literature.

Blends	PCE (%)	FF (%)	J_{SC} (mA cm^{-2})	V_{OC} (V)	Ref
PM6:BTP-S1	14.67 ± 0.24	70.88 ± 1.31	22.22 ± 0.31	0.932 ± 0.003	[12]
PM6:Y7	16.1 ± 0.2	74.3	25.2	0.872	[15]
PM6:Y6	16.27 ± 0.17	75.7 ± 0.9	25.57 ± 0.37	0.84 ± 0.01	[9]
PM6:Y6-BO	16.62 ± 0.08	76.8 ± 0.3	26.04 ± 0.15	0.832 ± 0.002	[11]
PM6:BTP-S9	17.42 ± 0.07	77.72 ± 0.46	26.48 ± 0.14	0.848 ± 0.003	[14]
PM6:BO-4Cl	17.28 ± 0.10	79.2 ± 0.3	25.87 ± 0.20	0.841 ± 0.002	[11]
PM6:BTP-eC9	17.87 ± 0.10	78.37 ± 0.74	27.12 ± 0.19	0.845 ± 0.003	[13]
PM6:L8-BO	17.97 ± 0.18	80.5 ± 0.9	25.66 ± 0.27	0.87 ± 0.01	[9]

Note:

(1) Most photovoltaic performance parameters are average values from literature except that FF, J_{SC} and V_{OC} of PM6:Y7-based devices are maximum values of devices, as report by reference[15].

Supplementary Table 3. Device structure and fabrication details of PM6:Y-type acceptor blend-based devices collected from literature.

Blends	D/A ratios	Cathode	Electron transport layer	Additive (volume content)	Annealing condition	Ref
PM6:BTP-S1	1:1	Ag	PFN-Br	CN (0.8%)	100 °C	[12]
PM6:Y7	1:1.1	Al	PDINO	CN (2%)	100 °C	[15]
PM6:Y6	1:1.2	Ag	PNDIT-F3N-Br	DIO (0.25%)	100 °C	[9]
PM6:Y6-BO	1:1.2	Ag	PFN-Br	CN (0.5%)	100 °C	[11]
PM6:BTP-S9	1:1.2	Ag	PFN-Br	DIO (0.25%)	80 °C	[14]
PM6:BO-4Cl	1:1.2	Ag	PFN-Br	DIO (0.5%)	100 °C	[11]
PM6:BTP-eC9	1:1.2	Ag	PFN-Br	DIO (0.25%)	80 °C	[13]
PM6:L8-BO	1:1.2	Ag	PNDIT-F3N-Br	DIO (0.25%)	100 °C	[9]

Note:
(1) All the devices have a conventional structure with ITO as anode, and PEDOT:PSS as hole transport layer.
(2) Additives: DIO: 1,8-diiodooctane; CN: Chloronaphthalene
(3) Annealing: 10 minutes

Supplementary Table 4. Photovoltaic parameters of binary OSC devices based on Y-type acceptors and various donor polymers collected from literature.

Donors	Y-type acceptors	PCE (%)	FF (%)	J_{SC} (mA cm^{-2})	V_{OC} (V)	Ref
PM6	Y6	16.61	76.0	25.91	0.84	[9]
	BO-4Cl	17.43	79.4	26.03	0.841	[11]
	BTP-eC9	18.0	77.95	27.57	0.845	[13]
	L8-BO	18.32	81.5	25.72	0.87	[9]
PM7	Y6	16.3	72.3	25.7	0.88	[18]
	BTP-eC9	16.06	76.03	24.36	0.867	[19]
	L8-BO	17.0	75.0	25.0	0.906	[18]
D18	Y6	17.84	75.5	27.31	0.865	[20]
	BTP-eC9	17.94	77.64	26.36	0.876	[21]
	L8-BO	17.7	78.5	24.9	0.907	[18]
D18-Cl	Y6	17.12	73.3	27.08	0.863	[6]
	BO-4Cl	17.1	73.7	25.8	0.90	[22]
	L8-BO	17.13	73.4	25.19	0.926	[23]

Note:
(1) All the photovoltaic performance parameters are those of the respective best-performance devices reported in literature.

Supplementary Table 5. Photovoltaic parameters of PM6:Y-type acceptor blend-

based devices prepared via layer-by-layer (LBL) approach collected from literature.

Blends	PCE (%)	FF (%)	J_{SC} (mA cm^{-2})	V_{OC} (V)	Ref
PM6:Y6	17.10	76.47	26.36	0.848	[24]
PM6:Y6-BO	17.2	77.5	26.2	0.847	[25]
PM6:BTP-eC9	17.48	78.1	26.65	0840	[26]
PM6:L8-BO	18.86	80.39	26.61	0.883	[27]

Note:
(1) All the photovoltaic performance parameters are those of the respective best-performance devices reported in literature.

Supplementary Table 6. Fitting results of azimuthally integrated GIWAXS profiles of Y-type acceptor neat films.

Films	Fitted peaks	q (Å^{-1})	FWHM (Å^{-1})	Area, A (a.u.)	A_2/A_1
BTP-S1	Peak 1	1.770	0.308	1.519	1.159
	Peak 2	1.483	0.630	1.761	
Y6	Peak 1	1.779	0.309	2.179	1.010
	Peak 2	1.434	0.616	2.200	
BTP-eC9	Peak 1	1.758	0.371	1.987	0.797
	Peak 2	1.457	0.545	1.584	
L8-BO	Peak 1	1.724	0.445	2.002	0.703
	Peak 2	1.353	0.682	1.408	

Note:
(1) Fitted peaks 1 and 2 correspond to ordered and disordered structures, respectively[9].
(2) FWHM: Full width at half maximum of fitted peaks.
(3) A_2/A_1: Ratio of the integrated area of peak 2 to that of peak 1.

Supplementary References

1 Mahadevan, S. *et al.* Assessing intra- and inter-molecular charge transfer excitations in non-fullerene acceptors using electroabsorption spectroscopy. *Nat. Commun.* **15**, 2393 (2024).
2 Kupgan, G., Chen, X. K. & Brédas, J. L. Molecular packing of non-fullerene acceptors for organic solar cells: Distinctive local morphology in Y6 vs. ITIC derivatives. *Mater. Today Adv.* **11**, 100154 (2021).
3 Xing, Z. *et al.* Improved Structural Order and Exciton Delocalization in High-Member Quasi-Two-Dimensional Tin Halide Perovskite Revealed by Electroabsorption Spectroscopy. *J. Phys. Chem. Lett.* **14**, 4349-4356 (2023).
4 Chan, C. C. S. *et al.* Quantification of Temperature-Dependent Charge Separation and Recombination Dynamics in Non-Fullerene Organic Photovoltaics. *Adv. Funct. Mater.* **31**, 2107157 (2021).
5 Zeng, A. *et al.* A Chlorinated Donor Polymer Achieving High-Performance Organic Solar Cells with a Wide Range of Polymer Molecular Weight. *Adv. Funct. Mater.* **31**, 2102413 (2021).
6 Ma, X. *et al.* Approaching 18% efficiency of ternary organic photovoltaics with wide bandgap polymer donor and well compatible Y6 : Y6-1O as acceptor. *Natl. Sci. Rev.* **8**, nwaa305 (2021).
7 Wang, Z. *et al.* The role of interfacial donor–acceptor percolation in efficient and stable all-polymer solar cells. *Nat. Commun.* **15**, 1212 (2024).
8 Wang, R. *et al.* Charge Separation from an Intra-Moiety Intermediate State in the High-Performance PM6:Y6 Organic Photovoltaic Blend. *J. Am. Chem. Soc.* **142**, 12751-12759 (2020).
9 Li, C. *et al.* Non-fullerene acceptors with branched side chains and improved molecular packing to exceed 18% efficiency in organic solar cells. *Nat. Energy* **6**, 605-613 (2021).
10 Zhang, K. *et al.* Triggering favorable energy landscape: a general approach towards highly efficient and photostable organic solar cells. *Energy Environ. Sci.* **15**, 5261-5273 (2022).
11 He, C. *et al.* Asymmetric electron acceptor enables highly luminescent organic solar cells with certified efficiency over 18%. *Nat. Commun.* **13**, 2598 (2022).
12 Li, S. *et al.* Asymmetric Electron Acceptors for High-Efficiency and Low-Energy-Loss Organic Photovoltaics. *Adv. Mater.* **32**, 2001160 (2020).
13 Zhan, L. *et al.* Desired open-circuit voltage increase enables efficiencies approaching 19% in symmetric-asymmetric molecule ternary organic photovoltaics. *Joule* **6**, 662-675 (2022).
14 Li, S. *et al.* Unveiling structure-performance relationships from multi-scales in non-fullerene organic photovoltaics. *Nat. Commun.* **12**, 4627 (2021).
15 Cui, Y. *et al.* Organic photovoltaic cell with 17% efficiency and superior processability. *Natl. Sci. Rev.* **7**, 1239-1246 (2019).
16 Fu, Y. *et al.* Molecular orientation-dependent energetic shifts in solution-processed non-fullerene acceptors and their impact on organic photovoltaic performance. *Nat. Commun.* **14**, 1870 (2023).
17 Zhu, L. *et al.* Efficient Organic Solar Cell with 16.88% Efficiency Enabled by Refined Acceptor Crystallization and Morphology with Improved Charge Transfer and Transport Properties. *Adv. Energy Mater.* **10**, 1904234 (2020).
18 Zhu, L. *et al.* Single-junction organic solar cells with over 19% efficiency enabled by a refined double-fibril network morphology. *Nat. Mater.* **21**, 656-663 (2022).
19 Liu, S. *et al.* Efficient Dual Mechanisms Boost the Efficiency of Ternary Solar

Cells with Two Compatible Polymer Donors to Exceed 19%. *Adv. Mater.* **36**, 2312959 (2024).
20 Liu, Q. *et al.* 18% Efficiency organic solar cells. *Sci. Bull.* **65**, 272-275 (2020).
21 Tang, J. *et al.* Wide Band-Gap Polymer Donors Functionalized with Unconventional Carbamate Side Chains for Polymer Solar Cells. *Angew. Chem., Int. Ed.* **61**, e202213252 (2022).
22 Li, D. *et al.* Co-crystallization of Fibrillar Polymer Donors for Efficient Ternary Organic Solar Cells. *ACS Mater. Lett.* **5**, 2065-2073 (2023).
23 Huang, T. *et al.* Dual-donor organic solar cells with 19.13% efficiency through optimized active layer crystallization behavior. *Nano Energy* **121**, 109226 (2024).
24 Liu, S. *et al.* High-Performance Pseudo-Bilayer Organic Solar Cells Enabled by Sequential Deposition of D18/Y6 Chloroform Solution. *ACS Applied Energy Materials* **6**, 5047-5057 (2023).
25 Fu, H. *et al.* A Generally Applicable Approach Using Sequential Deposition to Enable Highly Efficient Organic Solar Cells. *Small Methods* **4**, 2000687 (2020).
26 Zhang, Y. *et al.* Graded bulk-heterojunction enables 17% binary organic solar cells via nonhalogenated open air coating. *Nat. Commun.* **12**, 4815 (2021).
27 He, C. *et al.* Versatile Sequential Casting Processing for Highly Efficient and Stable Binary Organic Photovoltaics. *Adv. Mater.* **34**, 2203379 (2022).